NUCL SCI TECH (2021) 32:51
https://doi.org/10.1007/s41365-021-00882-2

Simulation study on performance optimization of a prototype scintillation detector for the GRANDProto35 experiment

Xiang-Li Qian[1] · Hui-Ying Sun[1] · Cheng Liu[2] · Xu Wang[1] · Olivier Martineau-Huynh[3]

Received: 24 December 2020 / Revised: 19 March 2021 / Accepted: 25 March 2021 / Published online: 18 May 2021

Abstract As a proposed detector, the giant radio array for neutrino detection (GRAND) is primarily designed to discover and study the origin of ultra-high-energy cosmic rays, with ultra-high-energy neutrinos presenting the main method for detecting ultra-high-energy cosmic rays and their sources. The main principle is to detect radio emissions generated by ultra-high-energy neutrinos interacting with the atmosphere as they travel. GRAND is the largest neutrino detection array to be built in China. GRANDProto35, as the first stage of the GRAND experiment, is a coincidence array composed of radio antennas and a scintillation detector, the latter of which, as a traditional detector, is used to perform cross-validation with radio detection, thus verifying the radio detection efficiency and enabling study of the background exclusion method. This study focused on the implementation of the optimization simulation and experimental testing of the performance of the prototype scintillation detector used in GRANDProto35. A package based on GEANT4 was used to simulate the details of the scintillation detector, including the optical properties of its materials, the height of the light guide box, and position inhomogeneity. The surface of the scintillator and the reflective materials used in the detector was optimized, and the influence of light guide heights and position inhomogeneity on the energy and time resolutions of the detector was studied. According to the simulation study, the number of scintillator photoelectrons increased when changing from the polished surface to the ground surface, with the appropriate design height for the light guide box being 50 cm and the appropriate design area for the scintillator being 0.5 m^2. The performance of the detector was tested in detail through a coincidence experiment, and the test results showed that the number of photoelectrons collected in the detector was ~ 84 with a time resolution of ~ 1 ns, indicating good performance. The simulation results were consistent with those obtained from the tests, which also verified the reliability of the simulation software. These studies provided a full understanding of the performance of the scintillation detector and guidance for the subsequent operation and analysis of the GRANDProto35 experimental array.

Keywords GRANDProto35 · GEANT4 · Scintillation detector · Light guide height · Photoelectrons

This work was supported by the National Natural Science Foundation of China (Nos. 11705103 and 12005120).

✉ Hui-Ying Sun
sunhy@sdmu.edu.cn

✉ Cheng Liu
liuc@ihep.ac.cn

Xiang-Li Qian
qianxl@sdmu.edu.cn

1 School of Intelligent Engineering, Shandong Management University, Jinan 250357, China

2 Key Laboratory of Particle Astrophysics, Institute of High Energy Physics, Chinese Academy of Sciences, Beijing 100049, China

3 Sorbonne Universite, Universite Paris Diderot, Sorbonne Paris Cite, CNRS/IN2P3, LPNHE, Paris, France

1 Introduction

Ultra-high-energy cosmic rays (UHECRs), with energies of $\geq 10^{18}$eV, are the most energetically charged particles ever observed, although their origin remains unclear

[1]. They are probably extragalactic in origin and purportedly made in powerful cosmic accelerators; yet, neither is identified. The direct strategy to discover UHECR sources is to detect localized excesses from the arrival direction of UHECRs. However, cosmic-ray charged particles tend to be easily changed in terms of direction because of the effect of galactic and intergalactic magnetic fields at the time of traveling, which prevents us from precisely retracing their trajectories back to their sources. UHECRs interact with cosmic microwave background photons, thus lowering their energy compared to the original energy. Consequently, only a few UHECRs above 40 EeV can reach the Earth from distances beyond 100 Mpc—the Greisen–Zatsepin–Kuzmin cutoff [2, 3].

In contrast, the indirect strategy entails looking for EeV gamma rays and neutrinos produced by UHECRs. UHECRs interact with their accelerating sources and surrounding matter to produce ultra-high-energy (UHE) gamma rays and neutrinos, which can point back at their sources because they are not charged nor affected by cosmic magnetic fields during propagation. However, similar to UHECRs, interactions with the cosmic microwave background cause the UHE gamma rays to lose both energy and their original information. Gamma rays do not reach the Earth beyond 10 Mpc. Instead, they cascade down to GeV–TeV, which makes it difficult to disentangle the gamma rays produced in unrelated phenomena. However, UHE neutrinos barely interact with intergalactic matter during intergalactic propagation because of their small cross section; therefore, they present the best means for the observation of UHECRs. Figure 1 shows the propagation of UHECRs and the associated secondary particles from their sources to the Earth.

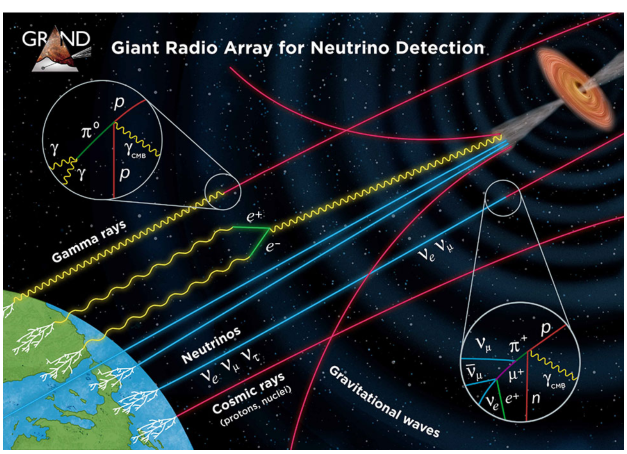

Fig. 1 (Color online) Schematic of the propagation of UHECRs from astrophysical sources to the Earth. Because of their interactions with cosmic photo backgrounds, cosmic rays produce UHE gamma rays (which cascade down in energy) and UHE neutrinos (which oscillate during propagation). All three UHE messengers may induce extensive air showers in the Earth's atmosphere

Because the cosmogenic neutrino flux is not constant and tiny fluxes are involved, an extremely sensitive neutrino detector array is needed for their discovery. The giant radio array for neutrino detection (GRAND), a proposed large-scale neutrino observation array planned in China, was designed for this purpose with the ultimate goal of discovering and studying the sources of UHECRs [4–6]. With GRAND, the sources of UHECRs may be better observed by combining cosmic rays, neutrinos, and gamma rays at different energies. Upon arrival at the Earth, UHECRs, gamma rays, and neutrinos initiate large particle showers in the atmosphere. The propagation of charged particles through the geomagnetic field may result in radio emissions. GRAND follows its principle to detect the ground footprint of the radio emission, using an array of 200,000 radio antennas distributed over an area of 200,000 km^2 and operating in the 50–200 MHz band. Because radio detectors are under novel development, and their performance parameters have to be tested by mature traditional detectors, the GRAND Cooperative Group established the GRANDProto35 experiment for testing.

The GRANDProto35 prototype coincidence array, as the first construction stage of the GRAND experiment, will lay the foundation for future stages. It is built based on the Tianshan Radio Experiment for Neutrino Detection project [7] located in the Tianshan Mountains in the Xinjiang province of China. It consists of 35 radio detectors and 24 scintillation detectors. A scintillation detector with high sensitivity and detection efficiency for cosmic-ray observation was used to perform cross-validation with radio detection [8]. The goal is to achieve an efficiency of $> 80\%$ for the radio detection of showers, with a background rejection that maintains the ratio of false positives to true positives to $< 10\%$. The GRANDProto35 coincidence array is arranged in a rectangle, and the entire array is 800 m long in the east–west axis and 2400 m long along the north–south axis. Because of the geomagnetic field, radio emission signals generated by cosmic rays perpendicular to the geomagnetic field direction are more concentrated; therefore, such an array arrangement is more conducive to the detection of air showers coming from the north. To improve the efficiency of cosmic-ray detection, scintillation detectors are inclined to the north.

The plastic scintillator is a unique detector that is used to detect and measure the properties of energetic charged particles in high-energy accelerators and nuclear and cosmic-ray physics experiments. Large-area plastic scintillators are commonly used as basic detector elements in cosmic-ray-induced extensive air shower experiments to measure the particle densities and their relative arrival times at the observational site. It is ideally suited for this purpose because of its rugged nature, fast response time

(~ 1 ns), and reasonable cost. For example, plastic scintillation detectors have been selected for MINOS [9], KASCADE-Grande [10], GRAPES-3 [11], AugerPrime [12], Tibet ASγ [13], and LHAASO [14].

There are several different designs for light collection in scintillation detectors: (1) The photons are collected by direct coupling of a photomultiplier tube (PMT) to one edge or one face of the scintillator [15]. Because the PMT cathode is much smaller than the scintillator area, only a small fraction of the emitted photons is collected. Furthermore, the nonuniform collection of photons is the primary factor influencing the variation in the detector response. (2) The scintillation light is collected using wavelength-shifting fibers, which have been designed for ATHLET [16], AugerPrime, etc. (3) By coupling the tapered plastic (adiabatic acrylic) light guide to the scintillator and PMT to improve detector uniformity, the addition of a plastic light guide to one end of the scintillator results in a tremendous loss of light and an increase in cost. In addition, the Cherenkov photons caused by charged particles in the light guide may cause spurious signals. To collect a large fraction of photon signals uniformly and with a good time resolution, a simple design of photon collection by the PMT mounted at a height below the scintillator is employed in GRANDProto35.

The main physical performance requirements for scintillation detectors used in GRANDProto35 are listed in Table 1 [17]. The experiment requires that the scintillation detector has high energy and time resolutions. Therefore, in this study, GEANT4 was used to simulate the light emitting, transmitting, and collecting processes of the scintillator. In addition, the simulation also accounted for how the shape of the light guide box and the position inhomogeneity of the detector influence the energy and time resolutions of the detector, thus optimizing the performance of the detector and meeting the requirements for physical indexes of the experiment.

The paper is constructed as follows: Sect. 2 describes the GEANT4 simulation process for the detector in detail, Sect. 3 compares the simulation and experimental results, and Sect. 4 details the optimization simulation and test results for the detector, i.e., the height of the light guide box and the position inhomogeneity of detector. Section 5 presents the conclusions of this study.

Table 1 Physical performance indexes of the scintillation detector used in GRANDProto35

Dynamic range (MIPs)	1–2000
Energy resolution (at MIP)	$<30\%$
Time resolution (ns)	<2
Detection efficiency	$>95\%$
Threshold (at MIP)	0.3
Detector normal orientation (zenith angle)	40°–60°

MIPs Minimum ionizing particles

2 GEANT4 simulation of the detector

A plastic scintillation detector uses the fluorescence generated by ionization and excitation of radiation in substances to detect ionizing radiation. The main working process is described as follows: (1) When the charged particles enter the scintillator, they interact with the scintillation crystal, thereby exciting and ionizing the atoms and molecules. (2) The excited atom is then deexcited to emit fluorescent photons with a wavelength in the visible band. (3) The light guide is used to collect as many scintillation photons to the PMT photocathode as possible, after which photoelectrons are emitted from the photocathode. (4) The photoelectrons multiply in the PMT to generate pulse signals. (5) The pulse signals are recorded and analyzed by electronics.

The best energy resolution was obtained by collecting only the maximum number of photons. For this reason, very good light collection is necessary; in this case, the parameters affecting light collection are an important criterion. For instance, light collection is largely influenced by different factors, including the type and reflectivity coefficient of reflective materials, the response of reflection and refraction of the photon at the boundary media, the roughness of the scintillator surface, the shape of the light guide, and the area of the scintillator. Therefore, these parameters need to be considered comprehensively in the detector simulation and design. In the past decades, various simulation studies on parameters influencing the light collection of scintillation detectors have been conducted [18, 19]. In terms of the studies on the surface reflectance properties, Janecek and Moses [20] proposed the use of measured reflectance data based on the experimental characterization of the angular reflection distribution of scintillators. Roncali and Cherry [21] proposed a different approach based on the three-dimensional measurements of crystal surfaces. Surface samples were scanned using three-dimensional atomic force microscopy and used to compute the reflectance properties of the crystal surfaces. These studies provided the reference methods and models for the design of the scintillation detector.

Optical Monte Carlo (MC) simulations are frequently used to predict the light distribution in scintillation crystals, together with light collection by photodetectors. Current MC simulation software such as DETECT [22], Litrani [23], GEANT4 [24, 25], and GATE [26] has been developed to perform such tasks. GEANT4 is a toolkit for simulating the passage of particles through matter. It can simulate the processes of particle ionizing in the scintillator and the transmission of scintillation light [27, 28]. All physical processes are simulated in detail based on the time when charged particles enter the detector at the time of detecting scintillation photons in photosensitive areas. This section introduces the setting of parameters in the GEANT4 simulation and the entire simulation process.

2.1 Geometric structural design of the detector

In this design, the scintillator is placed at the top of an inverted trapezoidal-shaped, light-tight container with reflective internal surfaces. The reflective surface guides the scintillation photons to the PMT after multiple diffuse reflections. Therefore, the detector mainly consists of a plastic scintillator, reflective coating, light guide device, light guide box (air light guide), and light collecting device (PMT). A stainless-steel housing was adopted for the detector. The dimensions of the optimized plastic scintillator were $707 \times 707 \times 20$ mm^3 (for a total area of 0.5 m^2), and the upper and lower dimensions of the light guide box housing were 730×730 mm^2 and 150×150 mm^2, respectively, with a vertical height of 500 mm. In view of the requirements for a large dynamic range of GRANDProto35, a dynode readout design was adopted for the PMT, for which the Hamamatsu R7725 model was selected. Because this experiment mainly focuses on cosmic rays with large zenith angles, an angle-adjustable baseplate was designed below the detector. Figure 2 shows a schematic of the scintillation detector.

2.2 Optical interface design for the scintillator

When the scintillation light produced in the scintillator encounters the edges of the scintillator, photons may be reflected or transmitted, and some of them may escape from the crystal. To strengthen the collection of light,

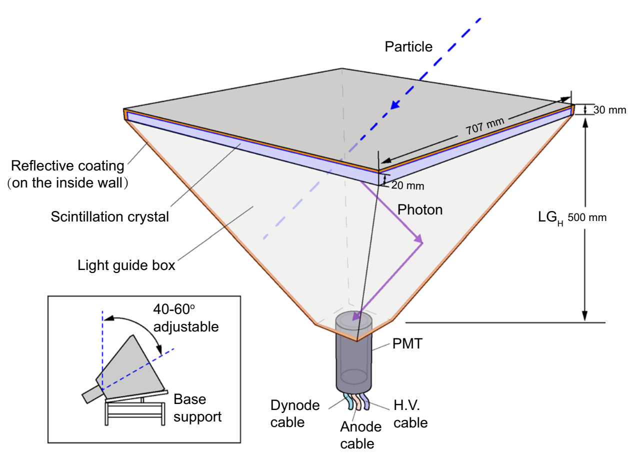

Fig. 2 (Color online) Schematic of the scintillation detector

Tyvek, a reflective material, was affixed to the upper and side surfaces of the scintillator, and the scintillator and the reflective material were tightly fitted by air. According to the refractive indexes of the scintillator and air, light at an emission angle within the range of the critical angle (θ_C) can escape from the scintillator and enter the light guide to reach the PMT. The remaining light escapes from the scintillator after some total internal reflections at the ends of the scintillator or is lost during the total internal reflections between the upper and lower interfaces of the scintillator, as shown in Fig. 3a. θ_c, the critical angle (39.2°) is calculated as follows:

$$\theta_c = \sin^{-1}\left(\frac{n_{\text{air}}}{n_{\text{scint}}}\right), \tag{1}$$

where n_{air} and n_{scint} refer to the refractive indexes of the air and scintillator, respectively.

To reduce the number of total internal reflections in the scintillator and increase the output of the light, the lower surface of the scintillator was ground, so that the photons to be collected may hit the ground surface at a large incident angle, thus escaping from the scintillator more easily. The process is illustrated in Fig. 3b. In practical applications, the upper surface is polished, the lower surface is ground, and the side surface is cut for the design of the scintillator.

2.3 Scintillator emission spectrum, PMT quantum efficiency, and Tyvek reflectivity

An EJ-200 scintillator (Eljen Technology, USA) was used as the plastic scintillator. It is characterized by a long optical attenuation length and fast time response, with a light yield of 10,000 photons/MeV. The light emission spectrum of the plastic scintillator and the quantum efficiency of the PMT photocathode are shown in Fig. 4. In the

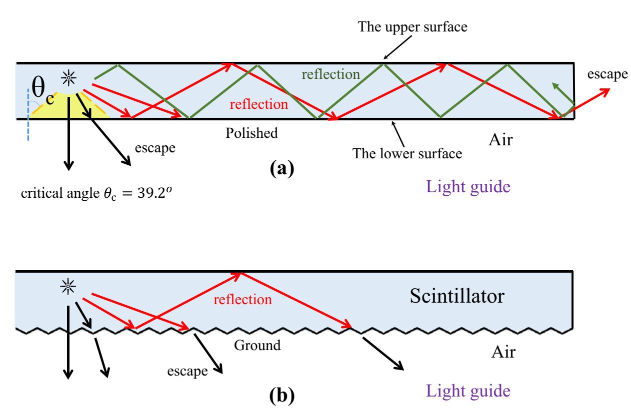

Fig. 3 (Color online) Schematic of the refraction and total internal reflection of scintillation light inside the scintillator and on the surface of the scintillator when **a** both the upper and lower surfaces are polished and **b** the upper surface is polished and the lower surface is ground

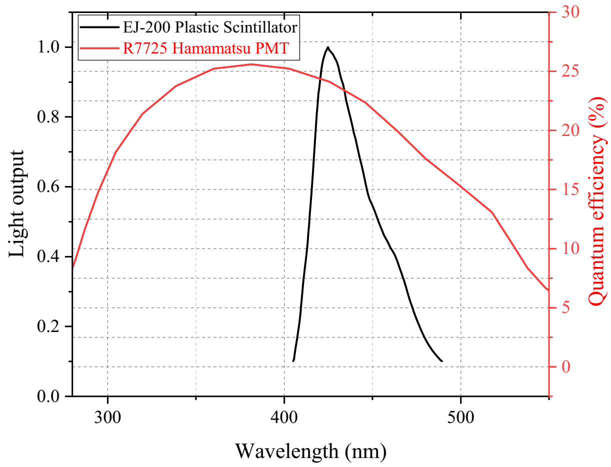

Fig. 4 (Color online) Emission spectrum of the EJ-200 plastic scintillator [29] and quantum efficiency of the PMT [30]

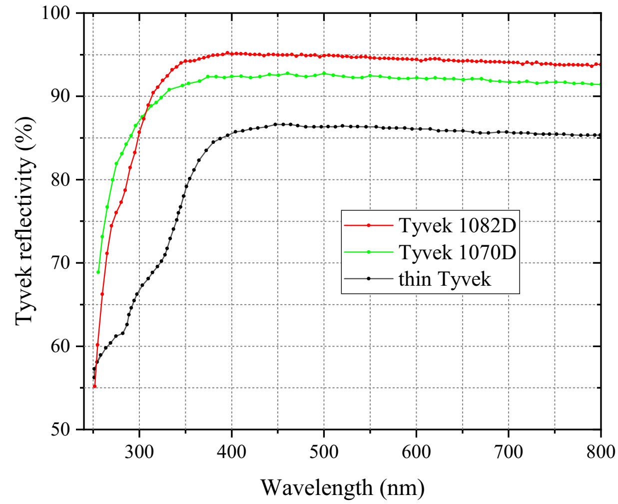

Fig. 5 (Color online) Reflectivity of different Tyvek models

figure, the black line indicates the EJ-200 emission spectrum, which is proportional to the probability of light emission at a given wavelength when the particles deposit energy, while the red line shows the quantum efficiency of the PMT at the corresponding wavelength. Within the scope of the emission spectrum of the scintillator, on average, the quantum efficiency of the PMT photocathode was $\sim$0.21. The performance parameters of the scintillator and PMT used in the simulation are listed in Table 2.

Tyvek, as the reflective material, was also affixed to the inner wall of the light guide box increase the detector's light collection efficiency. Figure 5 shows the reflectivity of different Tyvek models in air measured by the National Institute of Metrology, China. Because Tyvek 1082D clearly has the highest reflectivity among the three models, it was chosen. Its performance parameters are listed in Table 3. When the wavelength exceeded 380 nm, the reflectivity was $\sim$ 95%, and the reflectivity was high within the sensitive wavelength range of the scintillator and PMT. All of these performance parameters were digitized and added to the GEANT4 code to perform the simulation properly.

Table 2 Characteristic parameters of the scintillator and PMT used in the simulation

EJ-200 material properties	
Light output (% anthracene)	64
Scintillation efficiency (photons/MeV)	10,000
Wavelength of maximum emission (nm)	425
Light attenuation length (cm)	380
Density (g/cm^3)	1.023
Refractive index	1.58
PMT (R7725)	
Effective photocathode diameter (mm)	51
Transit time spread (ns)	1.85
Quantum efficiency	$\sim$ 0.21
Electron collection factor	0.6
Rise time (ns)	2.5
Fall time (ns)	3.4

2.4 Determination of optical simulation parameters

In GEANT4, there are two optical reflection models to be selected by the user: GLISUR and UNIFIED. These are used to describe the optical properties of medium surfaces. The GLISUR model, originating from GEANT3, defines the interface between two media as polished or ground, with only an adjustable parameter describing the roughness of the interface. The UNIFIED model is available for an accurate description of the optical process of the ground surface of various surface shapes over a long wavelength range.

Table 3 Tyvek 1082D specifications

Unit mass (g/m^2)	105
Thickness (μm)	275
Opacity	98.4%
Longitudinal elongation (N/(25.4 mm))	290
Transverse elongation (N/(25.4 mm))	330
Bursting strength (kPa)	1700

In the UNIFIED model, four types of surface reflections are possible: specular spike, specular lobe, backscatter, and Lambertian, as shown in Fig. 6. For specular reflection on an average surface, the reflected photons are reflected at the average surface normal. For backscatter reflection, the photons are reflected back in the direction from which they came. In Lambertian reflection, the photons are reflected with a Lambertian probability distribution, that is, into a cosine distribution around the average surface normal [20, 31].

It is assumed in the optical UNIFIED model that the surface of a medium is composed of an infinite number of "micro-facets." The entire surface is defined as an average surface, the micro-facets have their own normal directions, and the directions of all the micro-facets are averaged to obtain a direction. The included angle of the normal direction for the micro-facet and the normal direction for the average plane (α) follows a Gaussian distribution. The standard deviation of the distribution (σ_α) is used to describe the roughness of the surface. Each time a specular lobe interaction occurs, a micro-facet is randomly selected from this distribution, and a specular reflection is then calculated through the summation of all of the micro-facet orientations, as shown in Fig. 7. When a beam of photons with a certain momentum is incident on the surface of the medium, UNIFIED uses four parameters, namely, C_{sl}, the specular reflection probability of the micro-facet; C_{ss}, the specular reflection probability of the average surface; C_{bs}, the backscattering probability; and C_{dl}, the Lambertian reflection probability, to describe the radiant intensity of the surface. According to the model, $C_{sl} = 1$, and $\sigma_\alpha = 0$ corresponds to the case when the surface is completely polished.

Figure 8 shows 240× magnified images of the polished surface, the ground surface, and the cut surface of EJ-200 scintillator measured by using a VMS-1510F Video Measuring Instrument. Obviously, the three surfaces are different in roughness, and the polished surface of the scintillator is not completely polished; in that case, roughness was added in the simulation to a certain extent. The probabilities of specular spike reflection and backscatter reflection for these surfaces were very small; therefore, they were set to 0.

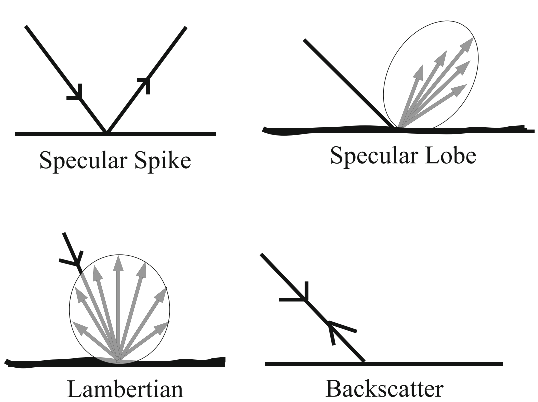

Fig. 6 Reflection types in the UNIFIED model, where the lengths of the different pointing arrows in the circles indicate radiant flux at different reflection angles [18]

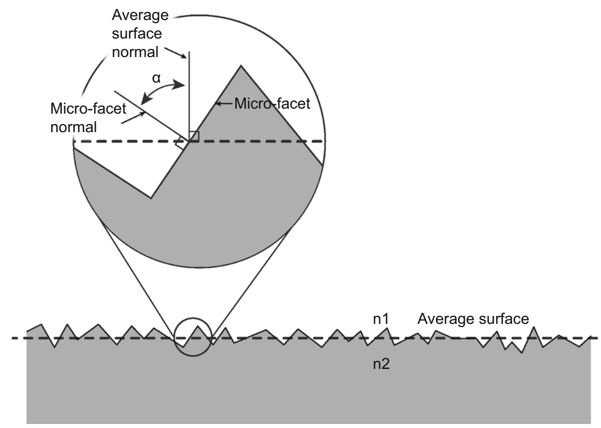

Fig. 7 Ground surface as defined in the UNIFIED model. The parameter σ_α defines the standard deviation of a Gaussian distribution consisting of α, the included angle between the micro-facet normal and the average surface normal

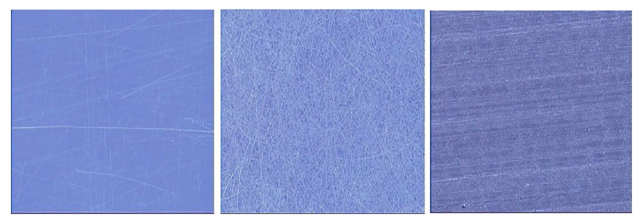

Fig. 8 (Color online) 240× magnified images of the polished surface (upper surface), ground surface (lower surface), and cut surface (side surface) of the scintillator used in the experiment

Tyvek reflective material is made of high-density polyethylene fiber, which is opaque and not smooth. Therefore, both specular and diffuse reflection can take place on the Tyvek surface, and diffuse reflection is the main component [32, 33]. In addition, the probability of backward scattering is very small ($C_{bs} = 0$). Tyvek exhibited a micro-faceted structure; therefore, the probability of specular spike reflection off it is also very small ($C_{ss} = 0$). The optical parameters of the scintillator surfaces and Tyvek surface used in the simulation are listed in Table 4.

2.5 Simulation of the PMT output signal

The number of photons emitted from the scintillator is proportional to the energy loss of the charged particles at a

Table 4 Optical parameters of the scintillator and Tyvek surfaces in the UNIFIED model used in the simulation

	C_{sl} (%)	C_{ss}	C_{dl} (%)	C_{bs}	σ_α
Polished surface	98.9	0	1.1	0	0.04
Ground surface	89	0	11	0	0.1
Cut surface	96.7	0	3.3	0	0.12
Tyvek surface	20	0	80	0	0.2

rate assumed to be one photon per 100 eV [34]. The angular distribution of the emitted light is isotropic. The time profile of scintillation emission is described by the following emission time (t_{emit}) probability function [35]:

$$n(t_{emit}) = \frac{n_f}{\tau_f} e^{-\frac{t_{emit}}{\tau_f}} + \frac{n_s}{\tau_s} e^{-\frac{t_{emit}}{\tau_s}}, \tag{2}$$

where τ_f refers to the fast decay time constants, τ_s represents the decay time of the slow component, and n_f and n_s denote the numbers of fast and slow components, respectively. Because the signal timing is determined at the leading edge in the discriminator, τ_f is the most important parameter for the simulation. In this simulation, τ_f is 2.1 ns and τ_s is 14.2 ns, where the emission time probability function can produce the same rise time as the scintillator light output.

The PMT produces a pulse signal if a single photoelectron is generated. The pulse waveform of a single photoelectron was simulated using the following time response function [36]:

$$v_i(t) = GC_e \frac{t^2 e^{-t^2/\tau^2}}{\int t^2 e^{-t^2/\tau^2}\, dt}, \tag{3}$$

where G is the gain of the PMT, C_e represents the charge-to-voltage conversion factor, and τ denotes the time constant of 2.5 ns, that is, the rise time of the PMT R7725 used for the detector. When a charged particle deposits its energy in the scintillator, optical photons are emitted, and multiple photoelectrons can be produced from the PMT. Because each photoelectron pulse arrives at the PMT at a different time, the output signal of the PMT can be obtained through the summation of the pulse waveforms of individual photoelectrons, which can be calculated using the following formula:

$$V_{PMT}(t) = \sum_{i=1}^{n_{pe}} v_i(t), \tag{4}$$

where n_{pe} represents the number of photoelectrons. Figure 9a, b shows a typical single photoelectron pulse waveform and the total PMT output signal waveform, respectively, in the simulation. The red dots in Fig. 9b represent the waveform of the simulated output pulse

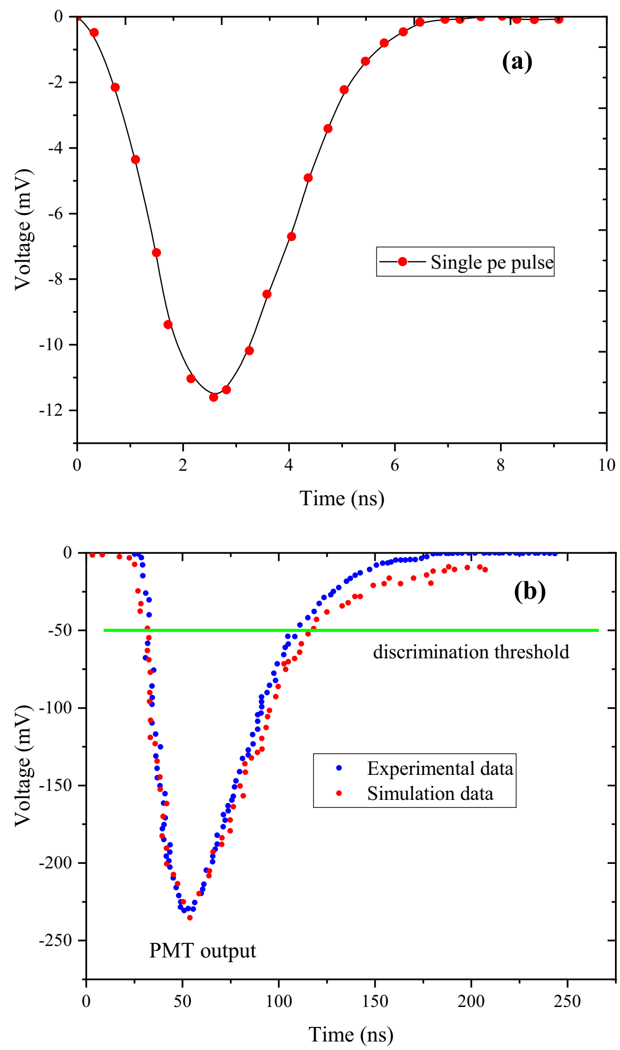

Fig. 9 (Color online) Photoelectron pulse waveforms: **a** PMT response for a single photoelectron and **b** PMT output pulse

signal. To make a comparison with the simulated output pulse, the experimental output pulse waveform of the optimized prototype detector was added. It can be clearly seen that the simulation data were consistent with the output signal obtained in the experiment, which proved the validity of the simulation for signal amplitude and time information. In the actual operation of the detector, the PMT output analog signal was amplified and converted into a digital signal by the front-end electronics, after which the charge and time information of the signal were obtained. Given the influence of noise, such as electronic noise, threshold discrimination was applied to the pulse in the GRANDProto35 electronics. In the simulation, the threshold voltage was set to -50 mV, corresponding to $\sim$ 0.3 MIPs. In fact, there was a time-walk effect when measuring time in this way. The effect was corrected in both the experiment and the simulation.

3 Comparison between simulation and experiment

The photoelectron energy spectrum and arrival time distribution of the detector can be obtained based on the GEANT4 simulation of the material composition, parameter setting, and the pulse signal output of the detector. To verify the final simulation results, a prototype detector was constructed using the geometric structure described in Sect. 2.1. (The height and area optimization of the detector are described in Sect. 4.) The details were then tested and analyzed. To eliminate the interference of noise and accurately measure the charge and time information of different positions on the detector surface, a $5 \times 5 \times 5$ cm^3 scintillator was placed above the prototype detector for the cosmic-ray coincidence event test. The testing principle is shown in Fig. 10. When passing through the 1/2 divider, the output signals of the coincidence scintillator and prototype scintillator are divided into two channels, one of which enters the analog-to-digital converters (CAEN V965) for charge measurement and the other is discriminated by a constant fraction discriminator (CAEN N843) and used as the start and stop signals of the time-to-digital converter (CAEN V775N) for time measurement.

To quantify the contribution of the Tyvek reflective materials to the increase in the light output, a comparative experiment was performed. The Tyvek material on the inner walls of the scintillator and light guide was changed to black paper. Four different packaging methods were tested for simulation: $Scin_{\mathrm{tyvek}}$-LG_{tyvek}, $Scin_{\mathrm{tyvek}}$-LG_{black}, $Scin_{\mathrm{black}}$-LG_{tyvek}, and $Scin_{\mathrm{black}}$-LG_{black}. Figure 11 illustrates the comparison of the photoelectron spectra between the simulation and experimental data collected by the PMT under $Scin_{\mathrm{tyvek}}$-LG_{tyvek} packaging. It is clear that, when the largest number of photoelectrons, $\sim$ 84 photoelectrons, are collected by the PMT under this packaging, the spectra of the simulation and experimental data are in good agreement. The energy resolution of the detector is defined as

$$\sigma = \frac{\tau}{2.355}, \tag{5}$$

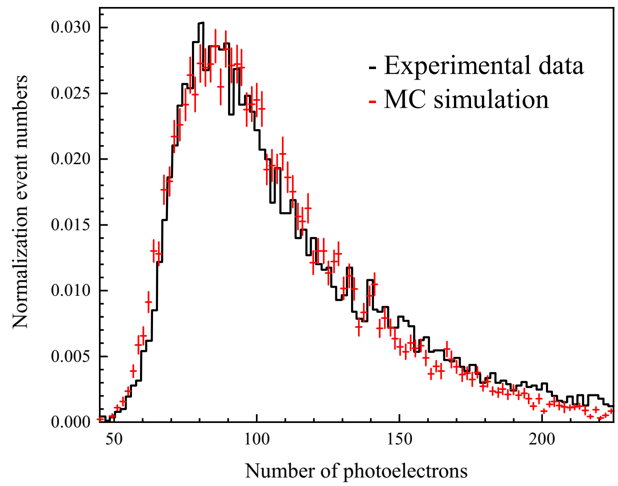

Fig. 11 (Color online) Comparison of photoelectron spectra from the simulation and experimental data under Tyvek packaging

where τ refers to the ratio of the full width at half maximum (ΔE) to the most probable value (E) of the photoelectron distribution, from which the energy resolution is calculated to be $\sim$ 25%. Table 5 shows the test results of all four packaging types. The experiments and MC simulations indicate that the design of Tyvek packaging around the scintillator and on the inside wall of the light guide box significantly improved the collection efficiency of the detector. Consequently, Tyvek packaging was used for subsequent simulations. To compare the difference of light output between the ground and the polished surfaces of the scintillator, a comparative test was also performed. The test results showed that the number of photoelectrons increased by $\sim$20% when the lower surface was changed to ground. Figure 12 shows the time difference distribution information detected by the prototype detector and the MC simulation data. It can be clearly seen that the experimental and simulation results are also consistent, and the time resolution is $\sim$ 1 ns.

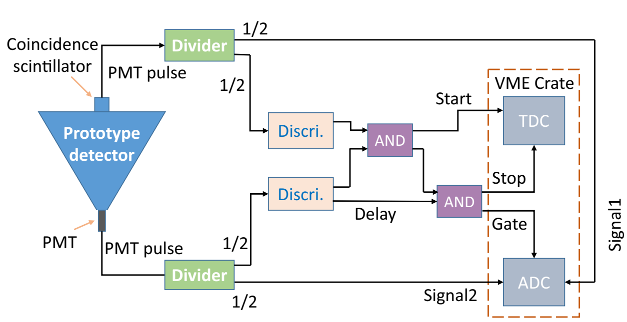

Fig. 10 (Color online) Block diagram for coincidence test of the prototype scintillation detector

Table 5 Number of scintillation detector photoelectrons (N_{pe}) measured under four different packaging types

Packaging type		N_{pe} (data)	N_{pe} (MC)	$\frac{\text{MC-data}}{\text{data}}$ (%)
Scintillator	Light guide			
Tyvek	Tyvek	84.0	86.1	2.5
Tyvek	Black paper	8.5	8.3	−2.3
Black paper	Tyvek	11.5	12.9	12.1
Black paper	Black paper	3.4	4.1	20.6

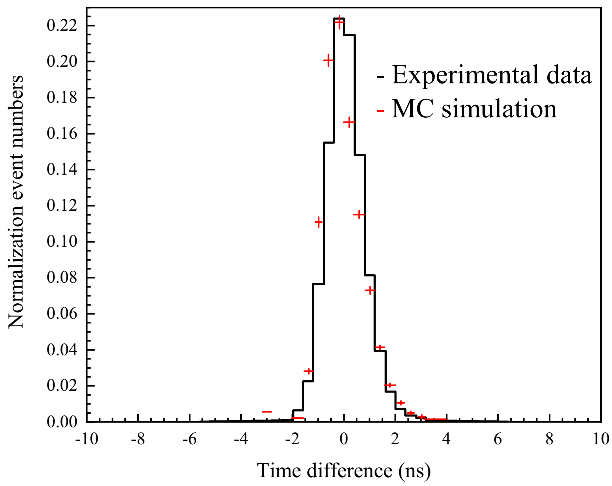

Fig. 12 Comparison of time difference distribution information between the simulation and experimental data under Tyvek packaging

4 Simulation of detector performance optimization

4.1 Influence of light guide heights on energy and time resolutions of the detector

The energy and time resolutions of the detector are closely related to the structure of the light guide box. Therefore, we simulated the optimization for the light guide heights under the condition of a fixed scintillator area (0.5 m^2). Muons are the dominant component of charged particles at sea level. Muon samples with energies of > 500 MeV were simulated and distributed over the entire surface of the detector. Figure 13 shows the distributions of photoelectrons collected by the PMT for different light guide heights (LG_H), that is, 10, 30, 50, 70, and 90 cm. It can be seen from the figure that the number of photoelectrons gradually decreased with the increase in the light guide height, with the most probable value decreasing from 134.7 to 56.6, and the energy resolution gradually becoming better to a certain extent. Table 6 lists the specific values of the number of photoelectrons and the energy resolutions at different light guide heights. Owing to the short propagation distance, more photons can be collected by the PMT for a low light guide height; however, the photoelectron distribution can be widened at the same time. This is largely due to the obvious position inhomogeneity at a low light guide height. For a high light guide height, the opposite is true.

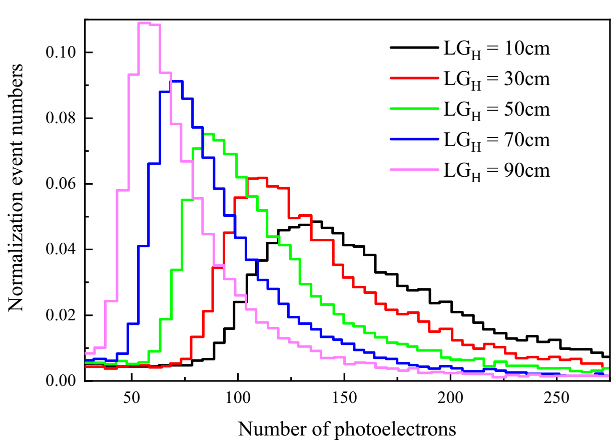

Fig. 13 (Color online) Number of photoelectrons measured at different LG_H values

Figure 14a shows the time resolution of the photons generated by the scintillator arriving at the PMT at different light guide heights, and Fig. 14b shows the total time distribution of all the photons generated by the scintillator after transmission through the light guide box. As can be seen from the two figures, the lower the light guide height, the less the time it took for the photons to reach PMT, and the better the time resolution. The reason for this is that, when the PMT was placed close to the scintillator, the photons had less distance to travel in the light guide box, and more photons arrived at approximately the same time; therefore, the time resolution was better, which was consistent with our expectation. The specific values of the time resolution are given in Table 6.

Based on the above results, we concluded that the lower the light guide height, the greater the number of collected photoelectrons. However, the energy resolution was poor, whereas the time performance was relatively good. Based on this, we selected the middle height (50 cm) as the light guide height. However, we still need to further consider the position response of the scintillator to determine the light guide height.

4.2 Influence of position inhomogeneity on energy and time resolutions of the detector

In the case in which the cosmic-ray particles hit different positions on the scintillator, the number of photoelectrons and time response will be different, which will affect the energy and time resolutions of the detector. Therefore, specific simulation and experimental studies

Table 6 Most probable value of the number of photoelectron and energy and time resolutions of the detector at different light guide heights

LG_H (cm)	10	30	50	70	90
N_{pe}	134.7	112.8	84.3	70.7	56.6
Energy resolution (%)	30.7	27.2	26.5	26.3	25.1
Time resolution (ns)	0.86	0.91	0.94	1.12	1.28

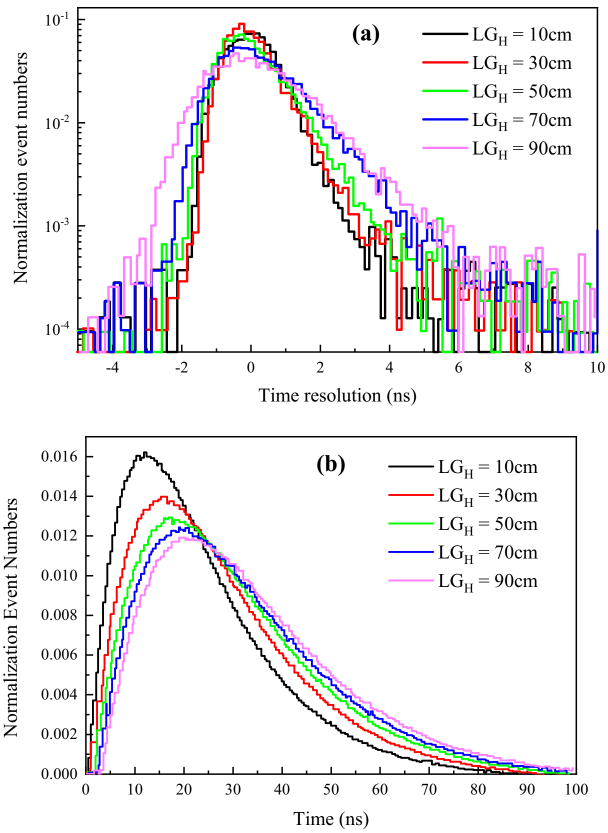

Fig. 14 (Color online) Time information measured at different LG_H values. **a** Time resolution of the detector. **b** Arrival time distribution of all photoelectrons

were conducted on the position homogeneity of the detector.

4.2.1 Simulation of position inhomogeneity

In the simulation, plumbing of different positions on the scintillator was used, different positions on the diagonal of the scintillator were selected, and a total of 18 points were tested. At each position, the photoelectron spectra at different light guide heights were simulated. Each photoelectron spectrum was fitted, and Landau and exponential convolution functions were adopted to obtain the most probable number of photoelectrons. The number of photoelectrons collected at the central point of the scintillator was regarded as 1, and the ratio of photoelectrons at other positions is defined as follows:

$$\text{ratio} = \frac{n_{\text{position}}}{n_{\text{center}}}. \tag{6}$$

According to the simulation results shown in Fig. 15, it is clear that, the closer to the edge of the scintillator one gets, the fewer the collected photoelectrons. This is because the photons generated at the edge of the scintillator were more easily lost during the propagation in the light guide box, and they cannot be received by the PMT. However, the higher the light guide height, the better the position homogeneity of the scintillator. When the height was 90 cm, the difference between the number of photoelectrons at the edge and that at the center of the scintillator was $\sim$ 15%. Furthermore, the position inhomogeneity changed more significantly as the light guide height decreased. These simulation results are consistent with expectations. Based on the results of the number of photoelectrons and energy and time resolutions of the scintillator under different light guide heights simulated in Sect. 4.1, a 50-cm light guide height was selected as optimal.

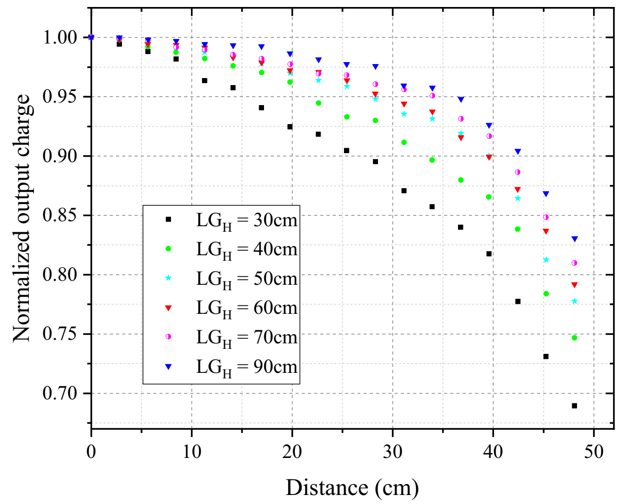

Fig. 15 Ratio of the output charge when the particles were incident at different positions of the scintillator to that at the central position

4.2.2 Influence of position inhomogeneity on the energy resolution of the detector

To verify the simulation, the coincidence test method used in Sect. 3 was adopted to test the position inhomogeneity of the scintillation detector. Points *A*–*G*, that is, a total of seven position points on the scintillator, were tested, as shown in Fig. 16a, and the light guide height was set to the optimum value (50 cm). Figure 16b shows the results of the comparison between the measured experimental data and the simulation. When the distance was $<$ 35 cm (the "*F*" position) from the central position of the scintillator, the number of photoelectrons decreases slowly; in contrast, when the distance is $>$ 35 cm, the number of photoelectrons decreases more quickly and the edge effect is more significant. The maximum inhomogeneity of the scintillation detector is $\sim$ 15%. Table 7 lists the number of photoelectrons, energy resolution, and position inhomogeneity results for all test points measured in both the experiment and simulation.

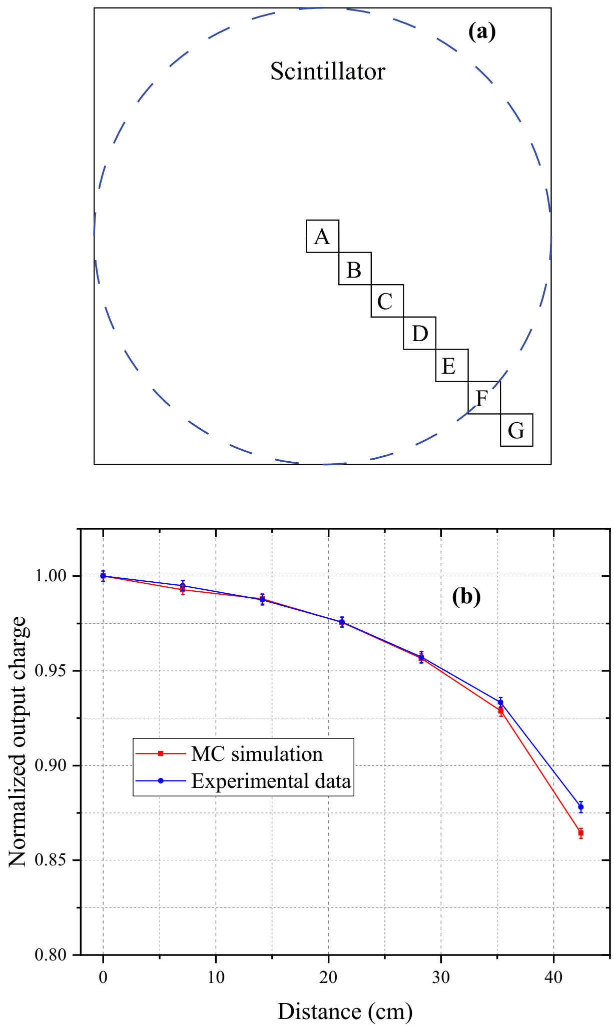

Fig. 16 Scintillator position inhomogeneity tests. **a** Schematic. **b** Comparison between simulation and experimental results

4.2.3 *Influence of position inhomogeneity on the time resolution of the detector*

Before a pulse signal enters the time-to-digital converter, it is discriminated by the discriminator, and the time-walk effect may appear [37]. When the leading edge of the pulse signal drops rapidly, the relation between the amplitude of the output signal and time can be expressed as follows:

$$V(T) = V_0\left(\frac{T - T_0}{T_{\mathrm{R}}}\right)^2, \tag{7}$$

where V_0 refers to the maximum value of the pulse signal, T_{R} represents the rise time of the signal, and T_0 denotes the start time of the signal. The time at the discrimination threshold, T_{th}, can be described as follows:

$$T_{\mathrm{th}} = T_{\mathrm{R}}\sqrt{\frac{V_{\mathrm{th}}}{V_0}} + T_0. \tag{8}$$

Because the charge of the pulse signal is proportional to the amplitude, that is, $Q \propto V_0$, the relation between T_{th} and Q can be expressed as follows:

$$T_{\mathrm{th}} = \frac{k}{\sqrt{Q}} + T_0, \tag{9}$$

where k is the time-walk factor. To accurately obtain the real-time resolution of the prototype scintillation detector, the charge and time were corrected, and the results showed that the time resolution of the detector can be improved by $\sim$ 20% through charge and time correction. Figure 17 shows the time resolution at different positions of the detector measured in the experiment. With an increase in the distance from the center of the detector, the time resolution at each point gradually deteriorated. However, the time resolutions were relatively good overall. The overall average time resolution is $\sim$1 ns, and the time-walk factor k obtained by fitting Eq. (9) is $\sim$ 78 ns $\cdot$ pC$^{1/2}$.

The experiment and simulation of position inhomogeneity showed that, with the increase in distance from the center, the number of photoelectrons gradually decreased and the time resolution also gradually deteriorated. Given the number of photoelectrons, energy resolution, and time resolution, the optimal area of the scintillation detector is 0.5 m^2 (i.e., the length of the side is 70.7 cm). In addition, the influence of scintillator thickness was also tested with different values, and the investigation showed that a

Table 7 Number of photoelectrons, energy resolution, and position inhomogeneity values of all test points measured in the experiment and calculated in the simulation

Performance	Position						
	A	B	C	D	E	F	G
Distance from center (cm)	0	7.07	14.14	21.21	28.28	35.35	42.42
N_{pe} (data)	84.0	83.58	82.94	81.96	80.40	78.39	73.75
N_{pe} (MC)	86.15	85.52	85.11	84.05	82.41	80.0	74.45
Homogeneity (data) (%)	100	99.50	98.75	97.58	95.73	93.33	87.80
Homogeneity (MC) (%)	100	99.28	98.80	97.56	95.67	92.87	86.43
Energy resolution (data) (%)	27.38	26.42	27.38	26.00	29.42	26.58	29.06
Energy resolution (MC) (%)	26.88	24.97	26.87	26.31	26.02	26.35	26.18

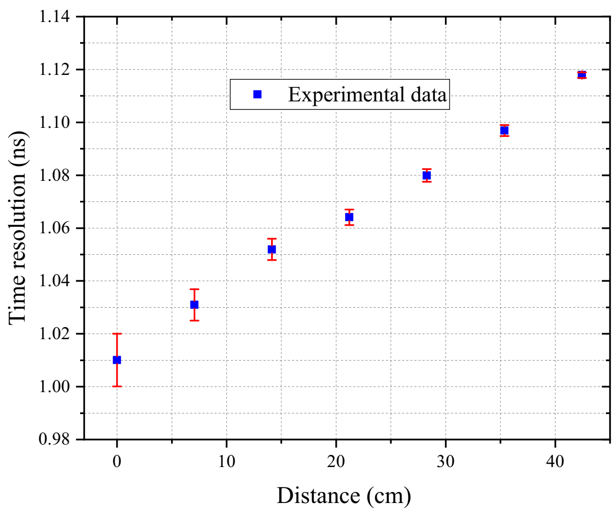

Fig. 17 Variation of time resolution with distance from the center of the detector

scintillator with 2 cm thickness could fulfill the requirements of the experiment.

5 Conclusion

As a coincidence array, the GRANDProto35 experimental array consists of radio antennas and a scintillation detector. The scintillation detector is mainly used for cross-validation with radio observations to improve the efficiency of radio detection for cosmic rays. The performance of the scintillation detector has an impact on the ability to detect UHECRs; therefore, it is necessary to conduct simulations and experiments to optimize the performance of the scintillation detector.

A specific GEANT4 simulation was conducted in which the optical properties of the materials used for the detector, height of the light guide, and position inhomogeneity of the detector were simulated. Based on the simulation study, to increase the number of photoelectrons collected in the detector, a ground surface of the scintillator was designed, and a Tyvek reflective material was added around the scintillator and on the inside wall of the light guide box. The light guide height and position inhomogeneity of the detector were studied in terms of the energy and time resolutions of the detector. According to the results, a light guide height of 50 cm and an area of 0.5 m^2 were optimal for the structural design of the detector. A series of verification experiments were performed, and the simulation results were found to be consistent with the experimental results, which verified the validity of our simulation. These results are very important for subsequent GRANDProto35 experiments, as well as for analyses of relevant physical targets.

Author Contributions All authors contributed to the study conception and design. Material preparation, data collection, and analysis were performed by Xiang-Li Qian, Hui-Ying Sun, Cheng Liu, Xu Wang, and Olivier Martineau-Huynh. The first draft of the manuscript was written by Xiang-Li Qian, and all authors commented on previous versions of the manuscript. All authors read and approved the final manuscript.

References

1. K. Kotera, A.V. Olinto, The astrophysics of ultrahigh-energy cosmic rays. Ann. Rev. Astron. Astr. **49**, 119 (2011). https://doi.org/10.1146/annurev-astro-081710-102620
2. K. Greisen, End to the cosmic-ray spectrum? Phys. Rev. Lett. **16**, 748 (1966). https://doi.org/10.1103/PhysRevLett.16.748
3. G.T. Zatsepin, V.A. Kuz'min, Upper limit of the spectrum of cosmic rays. Jetp. L. **4**, 78 (1966)
4. J. Álvarez-Muñiz, R.A. Batista, J. Bolmont et al., The giant radio array for neutrino detection (GRAND): science and design. Sci. China. Phys. Chem. **63**, 219501 (2020). https://doi.org/10.1007/s11433-018-9385-7
5. O. Martineau-Huynh, The giant radio array for neutrino detection, in *Paper Presented at the 36th International Cosmic Ray Conference* (Madison, WI, USA, July 24–August 1, 2019)
6. M. Tueros, Grand, a giant radio array for neutrino detection: objectives, design and current status. EPJ Web. Conf. **216**, 01006 (2019). https://doi.org/10.1051/epjconf/201921601006
7. D. Charrier, K.D. de Vries, Q.B. Gou et al., Autonomous radio detection of air showers with the TREND50 antenna array. Astropart. Phys. **110**, 15 (2019). https://doi.org/10.1016/j.astropartphys.2019.03.002
8. Q.B. Gou, O. Martineau-Huynh, J. David et al., The GRANDproto35 experiment, in *Paper Presented at the 35th International Cosmic Ray Conference* (Bexco, Busan, Korea 10-20 July, 2017)
9. D.G. Michael, P. Adamson, T. Alexopoulos et al., The magnetized steel and scintillator calorimeters of the MINOS experiment. Nucl. Instrum. Meth. A. **596**, 190–228 (2008). https://doi.org/10.1016/j.nima.2008.08.003
10. E.T. Antoni, W. Apel, F. Badea et al., The cosmic-ray experiment KASCADE. Nucl. Instrum. Methods A. **513**, 490 (2003). https://doi.org/10.1016/S0168-9002(03)02076-X
11. S.K. Gupta, Y. Aikawa, N.V. Gopalakrishnan et al., GRAPES-3-A high-density air shower array for studies on the structure in the cosmic-ray energy spectrum near the knee. Nucl. Instrum. Methods A. **540**, 311–323 (2005). https://doi.org/10.1016/j.nima.2004.11.025
12. A. Aab, P. Abreu, M. Aglietta et al., The pierre auger observatory upgrade-preliminary design report. http://arxiv.org/abs/1604.03637 (2016)
13. L.K. Ding, X.H. Ding, C. Fan et al., Tibet air shower array: results and future plan. J. Phys. Conf. Ser. **120**, 062024 (2008). https://doi.org/10.1088/1742-6596/120/6/062024
14. J. Zhao, J. Liu, X.D. Sheng et al., Design and performances of electromagnetic particle detector for LHAASO-KM2A. Chin. Phys. C. **38**, 036002 (2014). https://doi.org/10.1088/1674-1137/38/3/036002
15. P. Aguiar, E. Casarejos, J.A. Vilan et al., Geant4-GATE simulation of a large plastic scintillator for muon radiography. IEEE Trans. Nucl. Sci. **62**, 1233–1238 (2015). https://doi.org/10.1109/TNS.2015.2431297
16. G.I. Britvich, S.K. Chernichenko, A.P. Chubenko et al., The large scintillation charged particles detector of the Tien-Shan complex

"ATHLET". Nucl. Instrum. Methods A **564**, 225–234 (2006). https://doi.org/10.1016/j.nima.2006.03.042
17. X.L. Qian, X. Wang, H.Y. Sun et al., Simulation study on cosmic ray background at large zenith angle based on GRANDProto35 coincidence array experiment. Nucl. Sci. Tech. **32**, 1–11 (2021). https://doi.org/10.1007/s41365-020-00841-3
18. M. Kandemir, A. Cakir, Simulation and efficiency studies of optical photon transportation and detection with plastic antineutrino detector modules. Nucl. Instrum. Methods A **898**, 30 (2018). https://doi.org/10.1016/j.nima.2018.04.059
19. S. Scheu, H. Kaspar, P. Robmann et al., Studies on wrapping materials and light collection geometries in plastic scintillators. Nucl. Instrum. Methods A **567**, 345–349 (2006). https://doi.org/10.1016/j.nima.2006.05.153
20. M. Janecek, W.W. Moses, Simulating scintillator light collection using measured optical reflectance. IEEE Trans. Nucl. Sci. **57**, 964 (2010). https://doi.org/10.1109/TNS.2010.2042731
21. E. Roncali, S.R. Cherry, Simulation of light transport in scintillators based on 3D characterization of crystal surfaces. Phys. Med. Biol. **58**, 2185 (2013). https://doi.org/10.1088/0031-9155/58/7/2185
22. G.F. Knoll, T.F. Knoll, T.M. Henderson, Light collection in scintillation detector composites for neutron detection. IEEE Trans. Nucl. Sci. **35**, 872–875 (1988). https://doi.org/10.1109/23.12850
23. F.-X. Gentit, Litrani: a general-purpose Monte Carlo program simulating light propagation in isotropic or anisotropic media. Nucl. Instrum. Methods A **486**, 35–39 (2002). https://doi.org/10.1016/S0168-9002(02)00671-X
24. S. Agostinelli, J. Allison, K. Amako et al., GEANT4-a simulation toolkit. Nucl. Instrum. Methods A **506**, 250 (2003). https://doi.org/10.1016/S0168-9002(03)01368-8
25. J. Allison, K. Amako, J. Apostolakis et al., Geant4 developments and applications. IEEE Trans. Nucl. Sci. **53**, 270 (2006). https://doi.org/10.1109/TNS.2006.869826
26. G. Santin, D. Strul, D. Lazaro et al., GATE: a Geant4-based simulation platform for PET and SPECT integrating movement and time management. IEEE Trans. Nucl. Sci. **50**, 1516–1521 (2003). https://doi.org/10.1109/TNS.2003.817974
27. W.Z. Xu, Y.F. Liu, Z.Q. Tan et al., Geant4 simulation of plastic scintillators for a prototype μSR spectrometer. Nucl. Sci. Tech. **24**, 040401 (2013). https://doi.org/10.13538/j.1001-8042/nst.2013.04.011
28. S. Riggi, R. La Rocca, E. Leonora et al., GEANT4 simulation of plastic scintillator strips with embedded optical fibers for a prototype of tomographic system. Nucl. Instrum. Methods A **624**, 583–590 (2010). https://doi.org/10.1016/j.nima.2010.10.012
29. Eljen Technology, EJ-200 Plastic Scintillator. http://www.eljentechnology.com/images/products/data_sheets/EJ-200_EJ-204_EJ-208_EJ-212.pdf
30. Hamamatsu Photonics, 51 mm (2") Photomultiplier tube assembly R7725. http://www.hamamatsu.com/resources/pdf/etd/R7723_R7724_R7725_TPMH1315E.pdf
31. A. Levin, C. Moisan, A more physical approach to model the surface treatment of scintillation counters and its implementation into DETECT. IEEE Nucl. Sci. Conf. R. **2**, 702 (1996). https://doi.org/10.1109/NSSMIC.1996.591410
32. A. Filevich, P. Bauleo, H. Bianchi et al., Spectral-directional reflectivity of Tyvek immersed in water. Nucl. Instrum. Methods A **423**, 108 (1999). https://doi.org/10.1016/S0168-9002(98)01194-2
33. J. Arteaga-Velázquez, C. Vazquez-Lopez, A. Zepeda, A measurement of the diffuse reflectivity of 1056 Tyvek in air and water. Nucl. Instrum. Methods A **553**, 312 (2005). https://doi.org/10.1016/j.nima.2005.08.030
34. D. Clark, The intrinsic scintillation efficiency of plastic scintillators for 60Co gamma excitation. Nucl. Instrum. Methods **117**, 295 (1974). https://doi.org/10.1016/0029-554X(74)90412-1
35. C. Hawkes, M. Kuhlen, B. Milliken et al., Decay time and light yield measurements for plastic scintillating fibers. Nucl. Instrum. Methods A **292**, 329 (1990). https://doi.org/10.1016/0168-9002(90)90388-M
36. J. Nam, Y. Choi, D. Kim et al., A detailed Monte Carlo simulation for the Belle TOF system. Nucl. Instrum. Methods A **491**, 54 (2002). https://doi.org/10.1016/S0168-9002(02)01231-7
37. X.L. Qian, J.F. Chang, C.F. Feng et al., Calibration of pulse transit time through a cable for EAS experiments. Chin. Phys. C. **38**, 066202 (2014). https://doi.org/10.1088/1674-1137/38/6/066202